Dynamical features of the wake behind a pitching foil

Jian Deng,* Liping Sun, and Xueming Shao
State Key Laboratory of Fluid Power Transmission and Control, Zhejiang University, Hangzhou 310027, People's Republic of China
and Department of Mechanics, Zhejiang University, Hangzhou 310027, People's Republic of China
(Received 14 September 2015; published 10 December 2015)

As an extension of the previous study on the three-dimensional transition of the wake behind a pitching foil [Deng and Caulfield, Phys. Rev. E **91**, 043017 (2015)], this investigation draws a comprehensive map on the pitching frequency-amplitude phase space. First, by fixing the Reynolds number at Re = 1700 and varying the pitching frequency and amplitude, we identify three key dynamical features of the wake: first, the transition from Bénard–von Kármán (BvK) vortex streets to reverse BvK vortex streets, and second, the symmetry breaking of this reverse BvK wake leading to a deflected wake, and a further transition from two-dimensional (2D) wakes to three-dimensional (3D) wakes. The transition boundary between the 2D and 3D wakes lies top right of the wake deflection boundary, implying a correlation between the wake deflection and the 2D to 3D wake transition, confirming that this transition occurs after the wake deflection. This paper supports the previous extensive numerical studies under two-dimensional assumption at low Reynolds number, since it is indeed two dimensional except for the cases at very high pitching frequencies or large amplitudes. Furthermore, by three-dimensional direct numerical simulations (DNSs), we confirm the previous statement about the physical realizability of the short wavelength mode at $\beta = 30$ (or $\lambda_z = 0.21$) for Re = 1500. By comparing the three-dimensional vortical structures by DNSs with that from the reconstruction of Floquet modes, we find a good consistency between them, both exhibiting clear streamwise structures in the wake.

DOI: 10.1103/PhysRevE.92.063013 PACS number(s): 47.20.Ky, 47.27.Cn, 47.63.M−

I. INTRODUCTION

There is growing interest in biologically inspired flows due to their relevance in the design of micro-air vehicles (MAVs) and small unmanned underwater vehicles [1–3]. The flapping wing motion, which is a reasonable simplification of the kinematics of natural flyers and swimmers, is attractive due to its high efficiency and excellent maneuverability. In the last few years, significant work has gone into our understanding of the dynamics in the wake of a flapping wing [4–8]. An important parameter used in the study of flapping wings is the Strouhal number, defined as the product of the flapping frequency f and amplitude A divided by the forward moving speed U, i.e., $\mathrm{Sr}_A = fA/U$. It is well established that a thrust is generated at a sufficient Strouhal number, characterized by a reverse Bénard–von Kármán (BvK) vortex street in the wake [4,9]. In that case, if the flow is from left to right, the counterclockwise vortices move above the horizontal line, while the clockwise vortices move below. It has been revealed experimentally that the propulsive efficiency of a flapping foil peaks within a narrow interval $0.2 < \mathrm{Sr}_A < 0.4$ [4,5]. Observed cruise Strouhal numbers for a wide range of flying and swimming animals also lie on this interval [3], suggesting that natural selection has tuned animals for high propulsive efficiency.

By further increasing the Strouhal number, the deflection of the wake was observed, exhibiting that the clockwise and counterclockwise trailing edge vortices shed in pairs and propagate at an angle to the streamwise axis [10]. Interestingly, the asymmetric wake was also observed downstream of a purely heaving airfoil [11], as well as a purely pitching airfoil [12,13]. Since the deflected wake is usually accompanied with larger thrust and lift generation, it appears that to fully understand the underlying physics might be vital for the design and control of MAVs. It has been largely recognized that the initial choice of deflective direction, up or down, so-called dual modes, is determined by the initial conditions, i.e., the starting position and acceleration time [10]. However, it was also reported that small disturbances could trigger the switch between the modes in a random fashion [14,15].

Although the flow behind a flapping wing is naturally three dimensional [16–19], the quasi-two-dimensional (Q2D) hypothesis has been made by most previous studies [12,13]. It was assumed that for the flapping wing with a larger aspect ratio, a Q2D view can capture the main elements needed for an adequate description of the real three-dimensional flow. By setting up a foil of aspect ratio 4 pitching in a hydrodynamic tunnel [12], different regimes, characterizing the dynamics of the flow wake, were identified in the (Sr, A_D) phase space, where the dimensionless flapping amplitude A_D and the Strouhal number Sr are defined as $A_D = A/D$ and $\mathrm{Sr} = fD/U$ respectively, where a fixed length scale (D), the thickness of the foil, was chosen instead of the usual peak-to-peak amplitude (A) in the definition of Sr so that each degree of freedom of the flapping motion was represented in one nondimensional parameter. Two key dynamical features relevant to wake vortex systems engendered by flapping motion were evidenced: first, the transition from the well-known Bénard–von Kármán (BvK) wake to the reversed vortex street that signals propulsive wakes, and second, the symmetry breaking of this reverse BvK pattern giving rise to an asymmetric wake. It was also noted by a comparison of the zero-drag curve with the transition from a BvK vortex street to a reversed BvK pattern in the wake that, for increasing flapping amplitude or frequency, the reversal of the vortex street happens before the actual drag-thrust transition in almost all the parameter range studied in [12]. To correlate the wake dynamics of a flapping foil to the fishlike swimming and

*Corresponding author: zjudengjian@zju.edu.cn

 ©2015 American Physical Society

flapping flight in nature, they drew in the (Sr, A_D) phase space a region defined by $\mathrm{Sr}_A = 0.3 \pm 0.1$ (most likely selected by natural animals [3]), and showed that this region overlapped not only with the reverse BvK regime, but also the asymmetric region, which leads to the conjecture that animals using flapping-based propulsion must either exploit the creation of asymmetric wakes as part of their maneuvering techniques or, when cruising, avoid flapping regimes where the symmetry breaking of the reverse BvK street will occur.

To further explore the wake dynamics of a flapping foil, Ref. [20] conducted a Floquet stability analysis to quantify the inherent three-dimensional instability arising in the wake of a purely pitching foil. They reported that the transition from a two-dimensional wake to a three-dimensional wake occurred after the wake was deflected. Two distinct unstable spanwise-periodic modes were found, of which the subdominant long wavelength mode has certain points of similarity with the so-called mode A for a circular cylinder [21,22], while the short wavelength mode appears to have a period of the order of twice that of the base flow. In [20], a typical value of Sr, $\mathrm{Sr} = 0.22$, was selected and the Reynolds number was fixed at $\mathrm{Re} = 1500$; with varying pitching amplitude A_D the flow wakes were presented. It was stated that there were flows with certain flapping amplitudes, such as $A_D = 2.13$–2.53, where the wakes were deflected, yet $|\mu| < 1$ for all wave numbers, implying that wake deflection was not a sufficient condition for inherent three-dimensional instability of a flapping foil. Since only one Sr was studied in [17], it is not clear whether the sequencing for wake deflection and three-dimensional transition also applies to other Sr numbers. As suggested in [20], a systematic investigation in (Sr, A_D) parameter space is needed to promote our understanding of the relationship between inherent three-dimensional instability and wake deflection. It is also of interest to investigate by experiments or direct numerical simulations (DNSs) whether the short wavelength mode actually occurs.

The rest of the paper is organized as follows. First, we describe the simulation methodology for the base flow and the linear Floquet stability analysis strategy for studying the stability of a two-dimensional time-periodic base flow to three-dimensional disturbances. Descriptions of the results of our simulations are then organized into two parts. First, we discuss the wake dynamics within the (Sr, A_D) parametric space, aiming to draw a comprehensive map for identifying three transition boundaries: the transition from a BvK vortex street to a reverse BvK vortex street, the boundary between a symmetric wake and a deflected wake, and the transition from 2D to 3D wakes. Then, we present fully three-dimensional simulations at a specific parametric point, at which the previous study predicted a dominant short wavelength mode by Floquet analysis [20].

II. PROBLEM FORMULATION AND NUMERICAL METHODOLOGY

A. Definition of the problem studied

The basic setup is shown in Fig. 1. We consider a NACA0015 airfoil experiencing simultaneous pitching motions with a sinusoidal profile. The amplitude of pitching angle is denoted by θ_0, and the peak-to-peak amplitude of the trailing edge is denoted by A. We define the Reynolds number $\mathrm{Re} = Uc/\nu$, where c is the chord length, U is the streamwise velocity far upstream, and ν is the kinematic viscosity. We choose $\mathrm{Re} = 1700$ for our simulations, corresponding to $\mathrm{Re}_D = 255$ used in Ref. [12], defined as $\mathrm{Re}_D = UD/\nu$, where D is the thickness of the airfoil. The two parameters which characterize the wake dynamics are the appropriately scaled amplitude A_D, and frequency, or equivalently the Strouhal number Sr, defined as

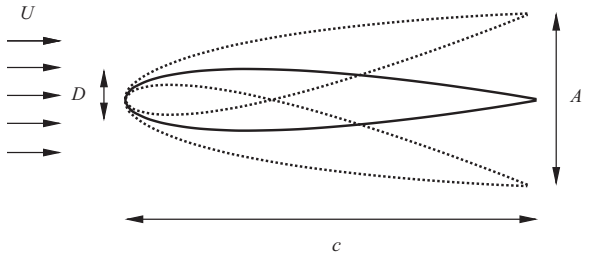

FIG. 1. Schematic view of the foil profile, which is symmetric, pivoted at the leading edge. D denotes the thickness of the foil, which is $0.15c$ for a NACA0015 airfoil.

$$A_D = A/D \quad \text{and} \quad \mathrm{Sr} = fD/U. \tag{1}$$

B. Solver for Navier-Stokes equations

The Navier-Stokes equations are solved using the finite volume method, assuming incompressibility [23]. The mass and momentum equations are solved on a moving grid domain using the arbitrary Lagrangian Eulerian (ALE) formulation. The region inside the circle of radius $5.0c$ and centered at the leading edge of the airfoil has a moving grid, accounting for the pitching motion, while the region outside has a fixed grid. The integral form of the governing (conservation) equations defined in an arbitrary moving volume V bounded by a closed surface S is

$$\frac{d}{dt}\int_V \rho \mathbf{U} dV + \oint_S \mathbf{ds}\cdot\rho(\mathbf{U}-\mathbf{U}_b)\mathbf{U} = \oint_S \mathbf{ds}\cdot(-p\mathbf{I}+\rho\nu\nabla\mathbf{U}), \tag{2}$$

where ρ is the density, $\mathbf{U}$ is the fluid velocity, $\mathbf{U}_b$ is the boundary velocity of a cell, p is the pressure, and ν is the kinematic viscosity. For details of the discretization and implementation of boundary conditions, one can refer to Ferziger and Peric [24].

The space discretizations are second-order upwind for the convection terms and central differences for the Laplacian terms, respectively. The temporal discretization is first-order implicit Euler. The pressure-velocity coupling is obtained using the PISO scheme [24]. The preconditioned conjugate gradient (PCG) method is used to treat the pressure equation and the preconditioned biconjugate gradient (PBiCG) method is used for the velocity equations. We set the boundary condition on the foil to be moving wall, with no flux normal to the wall. A constant velocity is imposed on the inlet boundary, and the pressure is set to a constant value at the outlet boundary.

For two-dimensional simulations, a rectangle is used as the outer boundary of our computational domain with the dimensions $20c \times 18c$. The domain is decomposed into two parts, of which the inner part is a circular zone with a diameter of $10c$. The cells in the inner part of the domain rotate rigidly with the pitching of the foil, interfacing with the outer part by a sliding circle. A mesh of 209 492 cells is used for the calculations. The same solver has been validated in Ref. [19], in which a flapping foil with prescribed motions was studied. For three-dimensional simulations, the 2D mesh is extruded to a three-dimensional domain. Distinguishing from those studies of the wings with finite-aspect ratio, here we note that the ends of the foil lie in the boundary planes, and the boundary planes (in which the ends of foil lie) are set to be translationally periodic.

C. Floquet stability analysis

To identify the transition boundary from 2D to 3D flows more efficiently, we conduct a linear Floquet stability analysis to study the stability of a two-dimensional time-periodic base flow to three-dimensional disturbances. The same code for solving the two-dimensional base flow field $[\bar{\mathbf{u}}(x,y,t), \bar{p}(x,y,t)]$ is modified to conduct the Floquet stability analysis. The base flow $[\bar{\mathbf{u}}, \bar{p}]$ is time periodic with period T such that with a three-dimensional perturbation, the total velocity and pressure are written as

$$\begin{aligned} \mathbf{u}(x,y,z,t) &= \bar{\mathbf{u}}(x,y,t) + \mathbf{u}'(x,y,z,t), \\ p(x,y,z,t) &= \bar{p}(x,y,t) + p'(x,y,z,t). \end{aligned} \tag{3}$$

After substituting the above form of the velocity and pressure fields into the Navier-Stokes equations and the continuity equation, we apply a conventional linearization under the assumption that the perturbations are sufficiently small and smooth so that all terms which are second order in perturbation quantities may be ignored. Therefore, we obtain linearized evolution equations for the perturbation flow field:

$$\frac{\partial \mathbf{u}'}{\partial t} = -\mathbf{L}(\mathbf{u}') - \nabla p' + \frac{1}{\mathrm{Re}}\nabla^2 \mathbf{u}', \quad \nabla \cdot \mathbf{u}' = 0, \tag{4}$$

and the linearized convective operator, $\mathbf{L}(\mathbf{u}')$, is given by

$$\mathbf{L}(\mathbf{u}') = (\bar{\mathbf{u}} - \mathbf{u_c}) \cdot \nabla_{xy} \mathbf{u}' + (\mathbf{u}' \cdot \nabla_{xy}) \bar{\mathbf{u}}, \tag{5}$$

where $\mathbf{u_c}(x,y,t)$ is the "cell" velocity of the moving mesh, and $\nabla_{xy} = (\partial/\partial x, \partial/\partial y, 0)$ is the two-dimensional gradient operator, since the base flow $\bar{\mathbf{u}} = [\bar{u}(x,y,t), \bar{v}(x,y,t), 0]$ and the cell velocity $\mathbf{u_c} = [u_c(x,y,t), v_c(x,y,t), 0]$ neither have components in nor depend on the z direction. Homogeneous Dirichlet boundary conditions are enforced on the perturbation velocities at the inflow and side boundaries (i.e., $\mathbf{u}' = \mathbf{0}$), while a homogeneous Neumann condition (i.e., $\partial \mathbf{u}'/\partial x = \mathbf{0}$) is imposed at the outflow.

Since we are interested in "inherent" three-dimensional instability of the base flow, we consider spanwise (z direction) periodic perturbations with spanwise wave number $\beta = 2\pi/\lambda_z$, where λ_z is the spanwise wavelength of the disturbance, and so we consider normal mode perturbations of the form

$$\begin{bmatrix} \mathbf{u}' \\ p' \end{bmatrix}(x,y,z,t) = \begin{bmatrix} \hat{\mathbf{u}} \\ \hat{p} \end{bmatrix}(x,y,\beta,t) e^{-i\beta z}, \tag{6}$$

where we make the dependence of the (in general complex) eigenfunction $[\hat{\mathbf{u}}, \hat{p}]$ on the wave number β explicit, and taking the real part is understood. The governing equations for each normal mode, which are naturally decoupled due to the linearization, are similar to Eq. (4), except for the replacement of the derivatives in the z direction with $\partial/\partial z = -i\beta$:

$$\begin{aligned} \frac{\partial \hat{u}}{\partial t} + (\bar{\mathbf{u}} - \mathbf{u_c}) \cdot \nabla_{xy} \hat{u} + \hat{\mathbf{u}} \cdot \nabla_{xy} \bar{u} &= -\frac{\partial \hat{p}}{\partial x} + \frac{1}{\mathrm{Re}}\left(\nabla_{xy}^2 \hat{u} - \beta^2 \hat{u}\right), \\ \frac{\partial \hat{v}}{\partial t} + (\bar{\mathbf{u}} - \mathbf{u_c}) \cdot \nabla_{xy} \hat{v} + \hat{\mathbf{u}} \cdot \nabla_{xy} \bar{v} &= -\frac{\partial \hat{p}}{\partial y} + \frac{1}{\mathrm{Re}}\left(\nabla_{xy}^2 \hat{v} - \beta^2 \hat{v}\right), \\ \frac{\partial \hat{w}}{\partial t} + (\bar{\mathbf{u}} - \mathbf{u_c}) \cdot \nabla_{xy} \hat{w} &= i\beta \hat{p} + \frac{1}{\mathrm{Re}}\left(\nabla_{xy}^2 \hat{w} - \beta^2 \hat{w}\right), \\ \frac{\partial \hat{u}}{\partial x} + \frac{\partial \hat{v}}{\partial y} &= i\beta \hat{w}. \end{aligned} \tag{7}$$

Applying the incompressibility constraint essentially to eliminate pressure, the partial differential equations (7) governing the evolution of a normal mode can be written symbolically as

$$\frac{\partial \hat{\mathbf{u}}}{\partial t} = \mathfrak{A}(x,y,t)\hat{\mathbf{u}}, \tag{8}$$

where the previously calculated base flow $\bar{\mathbf{u}}$ and cell velocity $\mathbf{u_c}$ are embedded in the linear differential (T-periodic) operator $\mathfrak{A}$. Once the partial differential equations are discretized in space, the velocity field can be represented as a vector whose elements consist of the velocity components at each grid point. Thus Eq. (8) is reduced to a system of ODEs of the form

$$\frac{d\hat{\mathbf{u}}}{dt} = \mathbf{A}(t)\hat{\mathbf{u}} \text{ with } \hat{\mathbf{u}}(t_0) = \text{specified}. \tag{9}$$

The discrete velocity vector $\hat{\mathbf{u}}$ contains the values of all three velocity components at the m grid points. Therefore, the length of the vector, n, equals $3m$. The matrix operator $\mathbf{A}(t)$ is simply the discretized version of $\mathfrak{A}$, and is an $n \times n$ T-periodic matrix.

Equation (9) has n linearly independent solutions given a set of n linearly independent initial conditions. Floquet analysis uses an $n \times n$ "fundamental solution matrix," $\Phi(t)$, where the n columns of the matrix are the n linearly independent solutions of the system. From integration of the system (9) over one period, we obtain

$$\Phi(t+T) = \Phi(t)\mathbf{C}, \tag{10}$$

where $\mathbf{C}$ is the constant $n \times n$ "monodromy" matrix, which is independent of the initial conditions [25]. The eigensolutions of the system (9) can be determined straightforwardly from the eigenvalues of $\mathbf{C}$.

Floquet's theorem [26] implies that the T-periodic operator $A(t)$ can be split into its periodic and exponentially varying parts. Since the fundamental solution operator $\mathbf{A}(t)$ is periodic, integrating over a single period T, the monodromy matrix $\mathbf{C}$ in Eq. (10) must capture the nonperiodic evolution, which can be expressed formally as $\mathbf{C} = \exp(\mathbf{B}T)$. The eigenvalues μ_n of $\mathbf{C}$ are known as the Floquet multipliers of the problem, governing the linear instability (if $|\mu_n| > 1$ for some n) or decay of the solution over each period. We note that the eigenvalues γ_n of $\mathbf{B}$ are known as the Floquet exponents, and are related to the

Floquet multipliers by

$$\mu_n = \exp(\gamma_n T), \tag{11}$$

and so instability occurs if the $\mathrm{Re}(\gamma_n) > 0$ for some n.

Since we are principally interested in instability onset, we do not solve for the complete set of eigenvalues μ_n, but rather utilize a numerical method identical to that of Refs. [27,28]. We numerically solve the initial value problem of Eqs. (7) over a several m_{bfp} base flow period T, renormalizing the perturbation fields at the end of each base flow period, until the magnitude of the Floquet multiplier reaches a constant value, suggesting that it is real, or fluctuates periodically around a constant value, suggesting that it also has an imaginary component. We estimate the magnitude of the largest Floquet multiplier by measuring the growth or decay of perturbation energy in the system. Here, we define a perturbation energy integrated over the entire domain volume V as

$$E(t) = \frac{1}{2}\int_V \sqrt{\hat{u}^2 + \hat{v}^2 + \hat{w}^2}\, dV. \tag{12}$$

Then, the absolute value of the eigenvalue with "maximum" magnitude can be approximated as

$$|\mu_{\max}| \approx \frac{E(t+T)}{E(t)}. \tag{13}$$

This method is equivalent to utilizing a power method [29] to compute the largest magnitude eigenvalues of $\mathbf{C}$, and m_{bfp} must be chosen to be sufficiently large to ensure the quality of the approximation. (More technical details about Floquet stability analysis and its application to hydrodynamic instability are presented in, for example, [27,28,30–32].)

III. RESULTS

The transition from well-known BvK wake to reverse BvK wake and the deflection of the reverse BvK wake of a pitching foil have been revealed experimentally, with the transition boundaries identified in a (Sr, A_D) phase space [12,13]. Another translational symmetry was found to break after the wake is deflected [20]. However, the study in Ref. [20] was constrained to a fixed Sr number, while it might be interesting to draw a comprehensive map on the (Sr, A_D) phase space. The primary purpose of the current study is to repeat the experiments [12] by numerics, though with a different profile of the foil. The current study mainly contributes to the research community by adding the third transition boundary of 2D to 3D flow to the (Sr, A_D) phase space.

A. Parametric study on the (Sr, A_D) space

At a fixed Reynolds number $\mathrm{Re} = 1700$, we perform a parametric study with varying Strouhal number and nondimensional flapping amplitude to identify different dynamical features in the (Sr, A_D) phase space. The phase map is shown in Fig. 2, with different symbols representing different types of wake. It is observed that the BvK-type wake lies primarily in the lower left region of the space but extends to higher Strouhal numbers for the lowest amplitude studied. The boundary between the BvK regime and the reverse BvK regime (blue line in Fig. 2) is defined in the (Sr, A_D) space when the central point of vortex, identified by the maximum value of the vorticity, lies on the center line. This boundary tends to an asymptotic value of $A_D \approx 0.5$ for $\mathrm{Sr} > 0.4$ so that a threshold amplitude value exists for the generation of a reverse BvK vortex street. We note that a different threshold amplitude value of $A_D \approx 0.6$ was reported in Ref. [12]. We conjecture that this disagreement is due to the fact that we consider a foil with different profile from that employed in Ref. [12], therefore they exhibit different hydrodynamic performance.

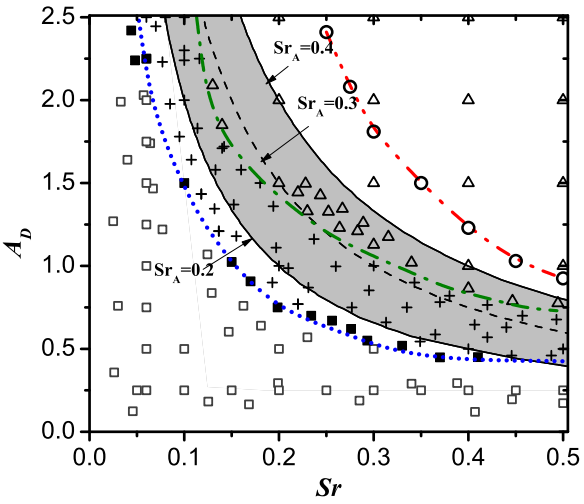

FIG. 2. (Color online) A_D vs Sr map for $\mathrm{Re} = 1700$. Computational points are labeled as □ : BvK wake; ■ : aligned vortices (2S wake); +: reverse BvK wake; △ : deflected reverse BvK street resulting in asymmetric wake; ○ : the points with neutral stability. Blue (dotted) line: transition between BvK and reverse BvK. Green (dash-dot) line: transition between reverse BvK and the asymmetric regime. Red (dash-dot-dot) line: transition between 2D and 3D wakes. The shaded area corresponds to the $\mathrm{Sr}_A = 0.3 \pm 0.1$ interval.

The reverse BvK regime is bounded on the other side by the transition (dash-dot line in Fig. 2) to asymmetric regime or the regime with deflected wakes. As mentioned in Sec. I, observed cruise Strouhal numbers for a wide range of flying and swimming animals lie within a narrow interval $0.2 < \mathrm{Sr}_A < 0.4$, where $\mathrm{Sr}_A = \mathrm{Sr}A_D$. We represent the previous interval with a region bounded by hyperbolas in the (Sr, A_D) phase space, as shown with a shaded area in Fig. 2. It is interesting to find that the reverse BvK to deflected wake transition lies in the region of $0.2 < \mathrm{Sr}_A < 0.4$, indicating that this interval overlaps not only with the reverse BvK regime, but also with the deflected wake regime. As conjectured in Ref. [12] animals using flapping-based propulsion must either exploit the creation of asymmetric wakes as part of their maneuvering techniques or, when cruising, avoid falling into the regimes where the symmetry breaking of the reverse BvK street occurs.

For a typical Sr number, $\mathrm{Sr} = 0.2$, we show snapshots of spanwise vorticity with varying A_D in Fig. 3, as well as time averaged streamwise velocity fields in Fig. 4. In Fig. 3, we observe three qualitatively different scenarios that the wake of a pitching foil undergoes: classic BvK vortex streets for $A_D = 0.25$ and $A_D = 0.50$, reverse BvK vortex streets for $A_D = 1.0$ and $A_D = 1.5$, and deflected vortex streets for $A_D = 2.5$. The

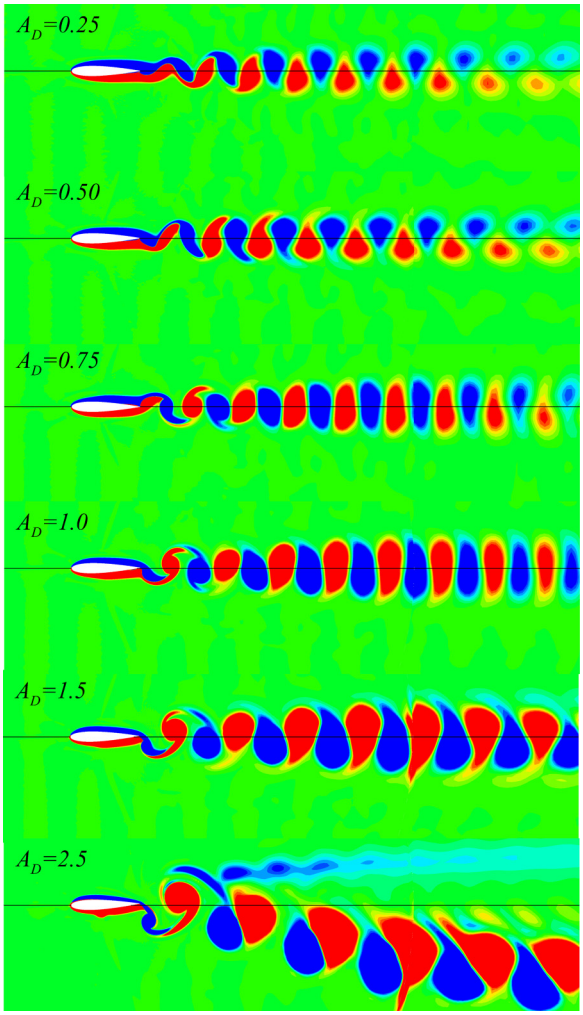

FIG. 3. (Color online) Instantaneous vorticity contours for the two-dimensional flow past a flapping foil at Re = 1700 and Sr = 0.2, and from top to bottom, $A_D = 0.25$, $A_D = 0.50$, $A_D = 0.75$, $A_D = 1.0$, $A_D = 1.5$, $A_D = 2.5$. Thirteen evenly spaced levels between −3 and 3 are plotted, with blue (dark grey) and red (light grey) denoting negative values and positive values respectively.

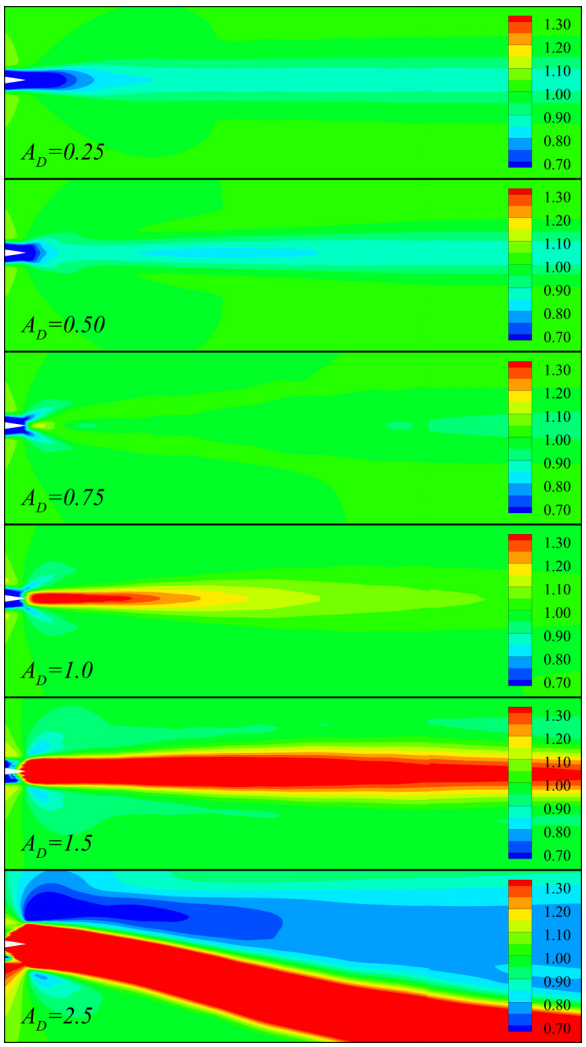

FIG. 4. (Color online) Mean flow field contoured by the time-averaged streamwise velocity, normalized by the velocity far upstream, U. From top to bottom, $A_D = 0.25$, $A_D = 0.50$, $A_D = 0.75$, $A_D = 1.0$, $A_D = 1.5$, $A_D = 2.5$. Blue (dark grey) and red (light grey) denote negative values and positive values respectively.

first two rows ($A_D = 0.25$ and $A_D = 0.50$) are typical cases showing drag wake with features resembling the BvK vortex street behind a circular cylinder, but with shedding frequency locked in to the pitching frequency. The vortices are shed continuously from each side of the foil, forming two rows of vortices in its wake, staying on the same side of the center line of the wake. For the wake far downstream, the energy of the vortices is consumed by viscosity, and the pattern dislikes that of the near wake, which is clearly shown for $A_D = 0.25$ and $A_D = 0.50$ in Fig. 3. Accordingly, the time averaged flows for these cases exhibit apparent velocity deficits behind the foil, as shown in Fig. 4. Increasing the flapping amplitude gives rise to a new pattern of the wake. For $A_D = 0.75$, the vortices of opposite signs align on the center line of the wake, forming a so-called 2S-type wake. Accordingly, the time averaged flow field for the 2S type shows that the mean streamwise velocity behind the foil has been recovered to the value of upstream velocity. For $A_D = 1.0$ and $A_D = 1.5$, the vortices shed on one side of the foil propagate in the wake on the other side of the center line characterizing the reserve BvK vortex street, which constitutes an accelerating flow, or a jet, behind the foil as represented by the time averaged flow fields as shown in Fig. 4.

As the amplitude is increased further, the reverse BvK propulsive vortex street departs slightly from the center line; as shown in Fig. 3 for $A_D = 2.5$, an apparent wake deflection occurs with a strong dipolar structure propagating obliquely to one side of the center line in each flapping cycle, while a much weaker single vortex is shed on the other side. For the corresponding time averaged flow field, the flow jet shifts from the center line, and a velocity deficit appears on the other side of the center line. Here, we note that the dipoles are deflected to the lower side the center line. By observing the initial stage of the vortical evolution, we support the statement about the mechanism of the side selection of deflection that it depends on the initial conditions [10]: the first dipoles entraining the flow behind the foil deflect the mean flow and attract the subsequent dipoles to follow its path.

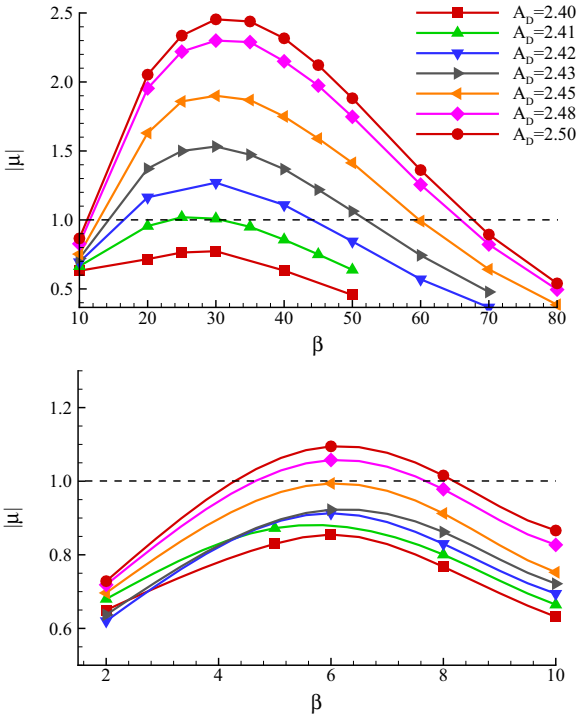

FIG. 5. (Color online) Variation of Floquet multiplier magnitude $|\mu|$ with wave number β. The line $|\mu| = 1$ corresponds to neutral stability of the Floquet modes.

Figure 2 also shows the transition boundary between 2D and 3D flow wake, which is the curve of neutral stability to infinitesimal three-dimensional perturbations. Here, the neutral stability means that the peak value of the magnitudes of the Floquet multipliers over the range of β equals to 1. The curve of neutral stability lies to the top right of the boundary from the reverse BvK street to the deflected wake, implying that the 2D-3D transition occurs after the wake deflection. It also suggests, at least in the parametric range studied here, that wake deflection is a necessary condition for inherent three-dimensional instability of a pitching foil. To show the sensitivity of the three-dimensional instability to the parameters in (Sr, A_D) space, we plot the variation with spanwise wave number β of the magnitude of the largest Floquet multiplier $|\mu_{\max}|$ for varying A_D in Fig. 5. For $A_D < 2.41$, the largest Floquet multiplier over the entire range of β is less than 1, indicating that the flow is stable to all infinitesimal three-dimensional perturbations. For $A_D > 2.41$, there is a range of wave numbers for which $|\mu| > 1$, indicating that the two-dimensional base flow is unstable to some linear three-dimensional disturbances. The wave number with the maximum growth rate is $\beta = 30$ and it corresponds to a nondimensional spanwise wavelength of $\lambda_z = 0.21$, nondimensionalized by the chord length c. A second local maximum can be observed at $\beta = 6$ ($\lambda_z = 1.05$). We find that at the critical flapping amplitude $A_D = 2.41$, the short wavelength mode is just becoming marginal, but the long wavelength mode is below the neutral line. As reported in Ref. [20], this suggests that the long wavelength mode is subdominant, and thus we do not expect it to be physically observed. To understand the flow structures of these two modes, one can refer to Ref. [20], which presents the perturbation streamwise

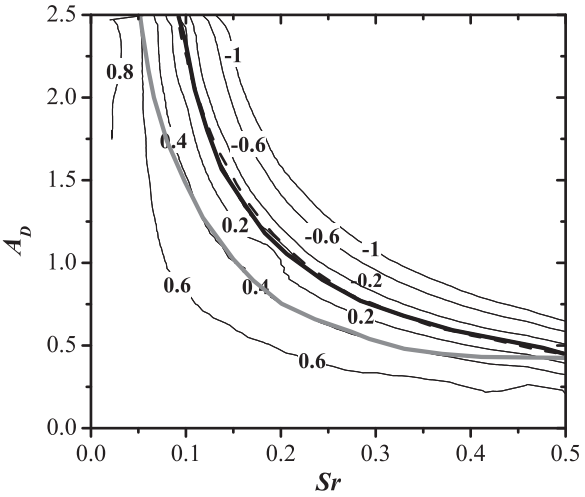

FIG. 6. Contours of a mean drag coefficient C_D. The back line corresponds to $C_D = 0$ where the drag-thrust transition occurs. The gray line is the transition from BvK to reverse BvK (dash-dot line in Fig. 2). The dashed line corresponds to $\mathrm{Sr}_A = 0.225$.

vorticity flow fields within a two-dimensional plane, as well as the reconstruction of three-dimensional topologies.

By integrating the pressure and viscous stress along the foil, we obtain the drag force F_D directly. In Fig. 6, we plot the contours of drag coefficient C_D in the (Sr, A_D) space, where C_D is calculated as

$$C_D = \frac{F_D}{\frac{1}{2}\rho U^2 c}. \tag{14}$$

The zero-drag curve marks the transition between drag and propulsive regimes (heavy back line in Fig. 6). We compare the zero-drag curve with the transition from a BvK vortex street to a reverse BvK wake (gray line in Fig. 6), showing that the zero-drag curve is located to the upper right of the transition boundary of BvK to reverse BvK pattern. This shift indicates that the reversal of the vortex street occurs actually before the drag-thrust transition in almost all the parameter range studies here, except for the high Sr numbers. As we can see, for $\mathrm{Sr} = 0.5$ the two curves approach each other. It implies that the thrust produced by the flapping motion is not enough to overcome all the drag composites, because it is apparent that the drag induced by viscous stress exits even when the foil stays still. We also note that the drag-thrust transition shown in Fig. 6 compares well with the $\mathrm{Sr}_A = 0.225$ curve (dashed line) that falls into the parametric scope of animal propulsion ($0.2 < \mathrm{Sr}_A < 0.4$, as introduced in Sec. I).

B. Three-dimensional DNS results

Floquet analysis has elucidated two unstable modes in the wake of a pitching foil [20]. The subdominant long wavelength mode has certain points of similarity with the so-called mode A behind a circular cylinder, while the short wavelength mode appears to have a period of the order of twice that of the base flow. There is also evidence presented that the long wavelength mode would not be observed physically because its growth rate is always less than the short wavelength mode. In order to verify these findings, and investigate the transition towards the

saturated state, a three-dimensional direct numerical study is performed for the parameters where the short wavelength mode is dominant and the long wavelength mode is also unstable. The Floquet analysis showed these criteria occur for Re = 1500, Sr = 0.22, and $A_D = 2.8$. It is noted that we choose this parameter point for direct comparison to Ref. [20], though it has left the parametric scope studied in Sec. III A.

Fully three-dimensional simulations are undertaken using the code introduced in Sec. II. To explore the wake evolution from two-dimensional to periodic flow to a fully three-dimensional saturated wake flow, the calculation places transitional periodic conditions on the two tip ending planes. A spanwise domain size of $0.42c$ is chosen, allowing two wavelengths for the short wavelength mode to fit inside the domain. Sixty spanwise slices are used for the computation. While this is somewhat minimal, full three-dimensional simulations are still computationally expensive, while it should still provide reasonable resolution for the saturated mode.

Figure 7 shows streamwise and spanwise vorticity isosurfaces for the DNS study once the flow has reached a quasiasymptotic state. It is apparent that the streamwise vortices originate in the region between the forming spanwise vortices in the near wake. First, the streamwise vortices arise on the edge of the newly forming spanwise vortex. As the pitching of the trailing edge, a spanwise vortex with opposite sign emerges below the preceding one, forming a dipolar structure, with the strong strain between the dipole intensifying the streamwise vortices. Then, as the dipoles propagate obliquely downstream, the streamwise vortices are stretched out and transferred to the emerging dipole of the next cycle. We observe that the streamwise vorticity swaps sign approximately every full shedding period. For comparison, we also plot a three-dimensional representation of the short wavelength mode in Fig. 8, in which the streamwise vortex structures resemble the isosurfaces shown in Fig. 7. There are two wavelengths shown in Fig. 7, indicating a selected spanwise wavelength of $0.21c$, consistent with the preferred wavelength of the Floquet mode, as shown in Fig. 8.

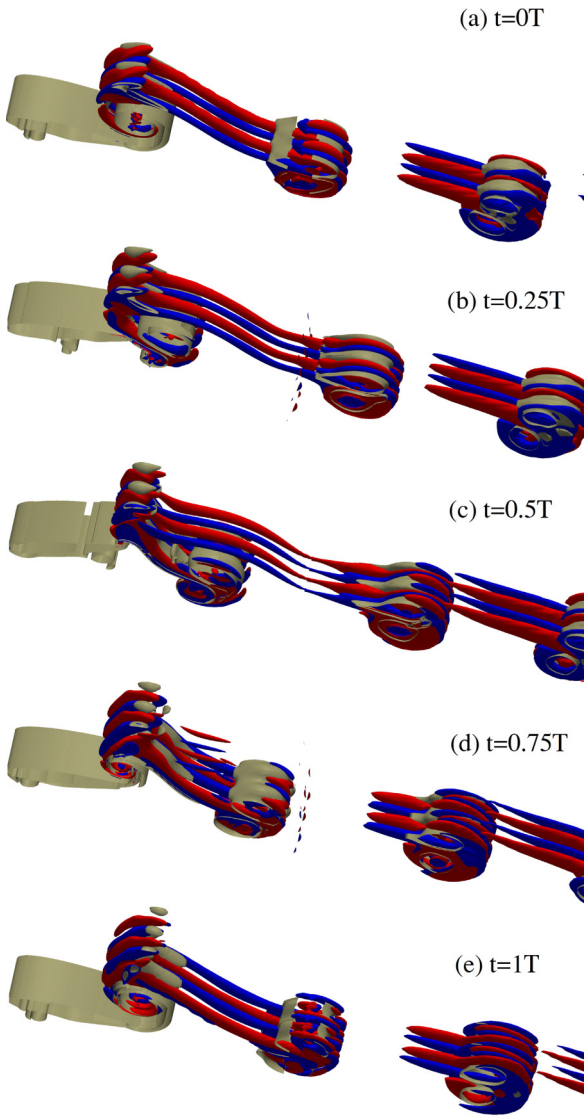

FIG. 7. (Color online) Three-dimensional DNS results for the isosurfaces of streamwise vorticity field ($\omega_x = \pm 6$) for the short wavelength mode at Re = 1500, $A_D = 2.8$, and $\beta = 30.0$. Five instants during a periodic cycle are shown. Blue (dark gray) and red (light gray) colors denote negative values and positive values respectively of ± 0.3 of the instantaneous maximum magnitude. Isosurfaces of spanwise vorticity ($\omega_z = \pm 6$) are also shown.

IV. CONCLUSIONS

We present a parametric study of the wake dynamics behind a pitching foil. By calculating on various flapping frequencies (Sr) and amplitudes (A_D), we identify three key dynamical features relevant to wake vortex systems engendered by purely pitching motion: first, the transition from the well-known Bénard–von Kármán (BvK) wake to the reverse BvK vortex street that signals the generation of thrust; second, the symmetry breaking of this reverse BvK wake gives rise to a deflected wake, which is asymmetric about the center line, and a further transition from two-dimensional (2D) wakes to three-dimensional (3D) wakes occurring after the wake deflection. It suggests that the wake deflection is a necessary condition for inherent three-dimensional instability of a pitching foil at least within the parameters studied in this paper. By using Floquet stability analysis to quantify the inherent three-dimensional instability arising in the wake, we find two apparently distinct unstable spanwise-periodic modes. The subdominant long wavelength mode which would not be observed physically has certain points of similarity with the so-called mode A for a circular cylinder, while the short wavelength mode appears to have a period of the order of twice that of the base flow. Besides, from the contours of drag coefficient, it is clear that the actual drag-thrust transition is located to the upper right of the transition boundary of BvK to a reverse BvK pattern, indicating that there exists a region where a reverse BvK pattern of positive drag value. Therefore, we state that a reverse BvK is not a sufficient condition for the thrust generation of a pitching foil. This finding is consistent with previous experiments.

Furthermore, the mechanisms of the transition from 2D wakes to 3D wakes are also investigated by three-dimensional direct numerical simulations (DNSs); we confirm the previous statement about the physical realizability of the dominant short wavelength mode. It is apparently shown that the streamwise

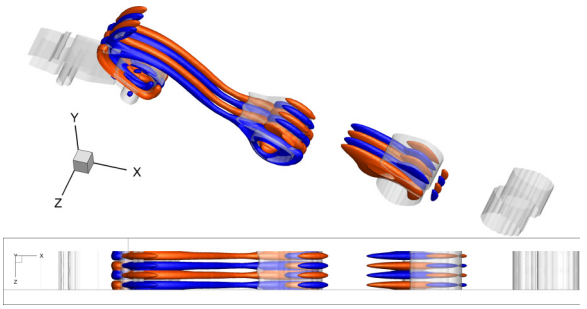

FIG. 8. (Color online) Isosurfaces of the streamwise vorticity field for the short wavelength mode for a simulation with Re = 1500, $A_D = 2.8$, and $\beta = 30.0$. Blue (dark gray) and red (light gray) colors denote negative values and positive values respectively of ±0.3 of the instantaneous maximum magnitude. Isosurfaces of the spanwise vorticity of the base flow are also shown in translucent light gray for positive (+6) and negative (−6) values to indicate the positions of the deflected BvK vortices. (Replotted from [20] with two spanwise repetitions presented.)

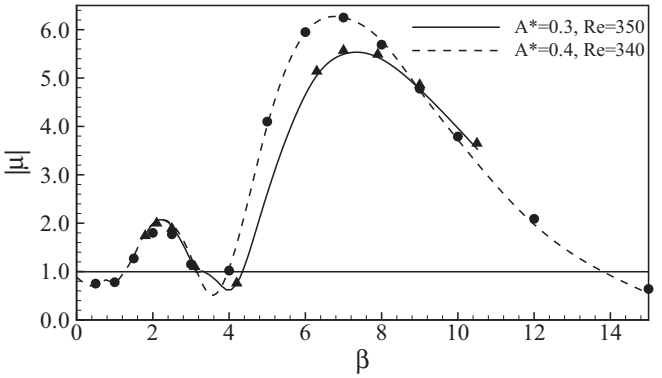

FIG. 9. Comparisons between our results and that by previous studies of Floquet multipliers $|\mu|$ as function of wave number β. The first case is at $A^* = 0.3$ and Re = 350, with the solid line representing the previous results in Ref. [34], and the present results are denoted by ▲. The second case is at $A^* = 0.4$ and Re = 340, with the dashed line representing the previous results in Ref. [35], and the present results are denoted by ●.

vortices originate in the region between the forming spanwise vortices in the near wake, and swap signs approximately every full shedding period. By comparing the three-dimensional vortical structures by DNSs with that from the reconstruction of Floquet modes, we find a good agreement between them, and both exhibit clear streamwise structures evolving in the wake. Thus we conjecture that the dominance of the linear instability is responsible for such a three-dimensional flow. Ideally, it would be advantageous to undertake simulations with larger spanwise computational domain to investigate whether the long wavelength mode will remain in the wake, though it is not surprising given the relative growth rate of the short wavelength mode and the long wavelength mode. And, this requires very long integration time and is thus expensive computationally. We are planning to investigate in detail the three-dimensional flow experimentally in the near future.

We note that a recent publication [33] provides a new view about the three-dimensional instabilities in wake flows in terms of centrifugal instabilities. For a circular cylinder performing high-amplitude rotatory oscillation, they declared that the possibility of three-dimensionalization in the wake could be determined by the Rayleigh discriminant, which reduces the complex procedure of identifying the transition boundary. It would be interesting to investigate whether the centrifugal instability can explain the current problem for a pitching foil, as we can observe indeed curved streamlines due to the dipoles within the deflected wake.

ACKNOWLEDGMENTS

We warmly thank Professor C. P. Caulfield at University of Cambridge for fruitful discussions. This work was supported by the National Natural Science Foundation of China (Grant No. 11272283) and Zhejiang Provincial Natural Science Foundation of China (Grant No. LY12A02006). J.D. gratefully acknowledges the hospitality of the Department of Applied Mathematics and Theoretical Physics, University of Cambridge.

APPENDIX: VALIDATION

The basic algorithms about Floquet analysis employed through this study have been used previously and shown to give accurate results [27,28]. However, most previous implementations were based on the spectral-element method with fixed grid systems. The Floquet stability analysis has seldom been employed for the study with moving grid, therefore an appropriate validation is necessary. Here, we undertake a Floquet stability analysis of the transition from the 2D to 3D wake of a transversely oscillating cylinder. A rectangular domain

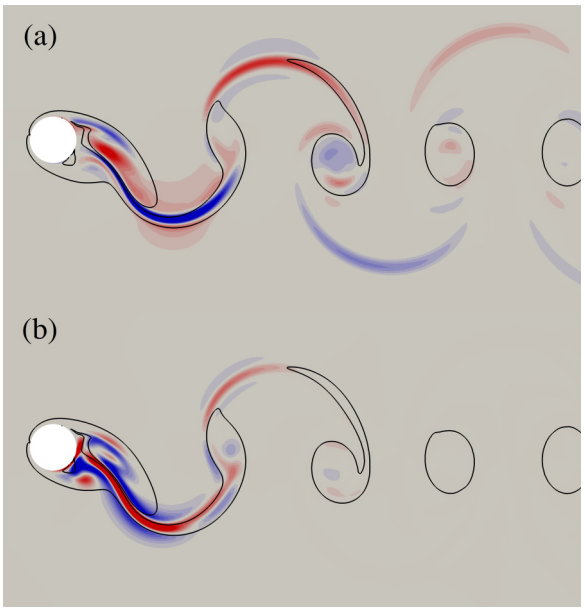

FIG. 10. (Color online) Instantaneous streamwise perturbation vorticity for the flow past an transversely oscillating cylinder. Blue (dark grey) and red (light grey) denote negative values and positive values respectively. The parameters are $A^* = 0.4$ and Re = 340, corresponding to our second validation case. (a) $\beta = 2.0$ for mode A, (b) $\beta = 7.0$ for mode B.

is used. The circular cylinder is placed inside the domain, with its center $16D$ away from the inlet, $25D$ away from the outlet, $16D$ away from the top boundary, and $16D$ away from the bottom boundary (D denotes the cylinder diameter). The boundary conditions are imposed as that of pitching foil. The smallest grid spacing near the cylinder is $0.01D$, and the grid is stretched out away from the cylinder surface. A time step $\triangle t = 0.001$ is used for the validation cases.

There are three parameters characterizing the flow behind an oscillating circular cylinder: $\mathrm{Re} = UD/\nu$, $A^* = A/D$, and the nondimensional oscillation frequency $f^* = fD/U$, where U is the free-stream velocity, D is the cylinder diameter, ν is the kinematic viscosity, A is the amplitude of oscillation, and f is the frequency of oscillation. We run two cases for $\mathrm{Re} = 350$ with $A^* = 0.3$ and $f^* = 0.2$, and for $\mathrm{Re} = 340$ with $A^* = 0.4$ and $f^* = 0.2$, following respectively Refs. [34,35]. We present the comparisons in Fig. 9. Plotted is the magnitude of the Floquet multiplier for the fastest growing mode over a range of wave numbers. The current results are in good agreement with previous studies [34,35], with two instability modes (modes A and B) identified. We note that the authors of Ref. [35] use $\sqrt{|\mu|}$ instead of $|\mu|$, so if we square root the Floquet multipliers accordingly, our results compare well with theirs.

To demonstrate how the perturbations of mode A and mode B respectively distribute in the wake, we choose two representative cases, as shown in Fig. 10. It shows that the forming primary vortex at the rear of the cylinder contains both positive and negative regions of perturbation vorticity, and a high concentration of perturbation in the high-strain region between vortices. Further downstream, the perturbation is most concentrated in the primary vortex cores. This qualitatively accords well with that reported in Ref. [35], and is also similar to the mode A in the wake of a fixed cylinder. Figure 10(b) shows the perturbation-field streamwise vorticity for mode B at $A^* = 0.4$ and $\mathrm{Re} = 340$ and $\beta = 7.0$. A significant difference between mode A and mode B is identified. For mode B, the perturbation-field streamwise vorticity repeats every half base period rather than every period as occurs for mode A.

[1] M. Triantafyllou, G. Triantafyllou, and D. Yue, Annu. Rev. Fluid Mech. **32**, 33 (2000).
[2] S. P. Sane, J. Exp. Biol. **206**, 4191 (2003).
[3] G. K. Taylor, R. L. Nudds, and A. L. Thomas, Nature (London) **425**, 707 (2003).
[4] J. Anderson, K. Streitlien, D. Barrett, and M. Triantafyllou, J. Fluid Mech. **360**, 41 (1998).
[5] D. A. Read, F. Hover, and M. Triantafyllou, J. Fluids Struct. **17**, 163 (2003).
[6] L. Schouveiler, F. Hover, and M. Triantafyllou, J. Fluids Struct. **20**, 949 (2005).
[7] M. F. Platzer, K. D. Jones, J. Young, and J. S. Lai, AIAA J. **46**, 2136 (2008).
[8] I. Fenercioglu and O. Cetiner, J. Fluids Struct. **31**, 92 (2012).
[9] M. M. Koochesfahani, AIAA J. **27**, 1200 (1989).
[10] K. Jones, C. Dohring, and M. Platzer, AIAA J. **36**, 1240 (1998).
[11] Z. Wei and Z. Zheng, J. Fluids Struct. **48**, 1 (2014).
[12] R. Godoy-Diana, J.-L. Aider, and J. E. Wesfreid, Phys. Rev. E **77**, 016308 (2008).
[13] R. Godoy-Diana, C. Marais, J.-L. Aider, and J. E. Wesfreid, J. Fluid Mech. **622**, 23 (2009).
[14] S. Heathcote and I. Gursul, Phys. Fluids **19**, 027104 (2007).
[15] D. J. Cleaver, Z. Wang, and I. Gursul, J. Fluid Mech. **708**, 349 (2012).
[16] R. Ramamurti and W. C. Sandberg, J. Exp. Biol. **205**, 1507 (2002).
[17] H. Dong, R. Mittal, M. Bozkurttas, and F. Najjar, AIAA J. **81**, 2005 (2005).
[18] M. Visbal, T. O. Yilmaz, and D. Rockwell, J. Fluids Struct. **38**, 58 (2013).
[19] J. Deng, C. Caulfield, and X. Shao, Phys. Fluids **26**, 043102 (2014).
[20] J. Deng and C. P. Caulfield, Phys. Rev. E **91**, 043017 (2015).
[21] C. Williamson, J. Fluid Mech. **328**, 345 (1996).
[22] C. H. Williamson, Annu. Rev. Fluid Mech. **28**, 477 (1996).
[23] H. Jasak, A. Jemcov, and Z. Tukovic, in *International Workshop on Coupled Methods in Numerical Dynamics* (Dubrovnik, Croatia, 2007), Vol. 1000, pp. 1–20.
[24] J. H. Ferziger and M. Perić, *Computational Methods for Fluid Dynamics* (Springer, Berlin, 2002), Vol. 3.
[25] G. Iooss, D. D. Joseph, F. Jehring, and P. Halmos, *Elementary Stability and Bifurcation Theory* (Springer, New York, 1980), Vol. 34.
[26] P. J. Schmid and D. S. Henningson, *Stability and Transition in Shear Flows* (Springer, New York, 2001), Vol. 142.
[27] J. Robichaux, S. Balachandar, and S. Vanka, Phys. Fluids **11**, 560 (1999).
[28] D. Richter, E. S. Shaqfeh, and G. Iaccarino, J. Non-Newtonian Fluid Mech. **166**, 554 (2011).
[29] L. S. Tuckerman and D. Barkley, *Bifurcation Analysis for Timesteppers* (Springer, New York, 2000).
[30] D. Barkley and R. D. Henderson, J. Fluid Mech. **322**, 215 (1996).
[31] D. Barkley, L. S. Tuckerman, and M. Golubitsky, Phys. Rev. E **61**, 5247 (2000).
[32] H. M. Blackburn and J. Lopez, Phys. Fluids **15**, L57 (2003).
[33] J. D'Adamo, R. Godoy-Diana, and J. E. Wesfreid, Proc. R. Soc. A **471**, 20150011 (2015).
[34] J. S. Leontini, M. Thompson, and K. Hourigan, J. Fluid Mech. **577**, 79 (2007).
[35] R. Gioria, P. Jabardo, B. Carmo, and J. Meneghini, J. Fluids Struct. **25**, 676 (2009).